

Investigating the response of wave-generated ripples to changes in wave forcing

Chuang Jin ^{a,*}, Giovanni Coco ^a, Rafael O. Tinoco ^b, J. Taylor Perron ^c, Paul M. Myrow ^d, Kimberly L. Huppert ^e, Heide Friedrich ^f, Evan B. Goldstein ^g, Zheng Gong ^h

^a School of Environment, Faculty of Science, University of Auckland, Auckland 1010, New Zealand

^b Department of Civil and Environmental Engineering, University of Illinois at Urbana-Champaign, Urbana, IL 61801, USA

^c Department of Earth, Atmospheric & Planetary Sciences, Massachusetts Institute of Technology, Cambridge, MA 02139, USA

^d Department of Geology, Colorado College, Colorado Springs, CO 80903, USA

^e Helmholtz Centre Potsdam, German Research Centre for Geosciences (GFZ), Potsdam 14473, Germany

^f Department of Civil and Environmental Engineering, University of Auckland, Auckland 1010, New Zealand

^g Department of Geography, Environment, and Sustainability, University of North Carolina at Greensboro, Greensboro, NC 27412, USA

^h State Key Laboratory of Hydrology-Water Resources and Hydraulic Engineering, Hohai University, Nanjing 210000, China

ARTICLE INFO

Article history:

Received 25 November 2019

Received in revised form 23 April 2020

Accepted 25 April 2020

Available online 03 May 2020

Keywords:

Ripples

Bedforms

Hysteresis

Defects

Critical Shields

ABSTRACT

Wave-generated ripples are macroscopic roughness elements that influence fluid flow and sediment transport. For a major group of ripples (orbital ripples), morphology (height and wavelength) is set by the wave conditions. In natural conditions, where wave forcing is highly variable, ripple morphology is frequently changing. We investigate the rate of morphological change after changes in wave conditions (i.e., wave height and period), using laboratory experiments with a step-change in wave forcing. The adjustment time of ripple morphology to new conditions -- the hysteresis time scale (hereafter referred to simply as hysteresis) -- is proportional to changes in wave orbital diameter, and the coefficient of proportionality differs for decreasing and increasing orbital diameter. When the Shields parameter is lower than a threshold (0.043), there is no change in ripple morphology (or changes are extremely slow). In addition, we find the presence of defects (irregularities from straight parallel crestlines) reduces the hysteresis time scale. The dependence of hysteresis on defect density implies that a larger density of defects results in faster ripple adjustment, confirming previous theoretical and numerical model results.

© 2020 Elsevier B.V. All rights reserved.

1. Introduction

Oscillatory ripples are quasi-sinusoidal sediment bed features that form under the action of waves in a variety of shallow-water environments. The presence of wave-generated ripples significantly increases bed roughness and near-bottom sediment transport (Davies and Thorne, 2005; Marieu et al., 2008), and affects wave dissipation (Ardhuin et al., 2003).

A great effort has been made to investigate the equilibrium characteristics of wave-generated ripples through laboratory experiments (e.g., Darwin, 1883; Ayrton, 1910; Hansen et al., 2001a, 2001b; Perillo et al., 2014; Ruessink et al., 2015; Perron et al., 2018; Wu et al., 2018; Yuan and Wang, 2018; Wang and Yuan, 2019), numerical simulations (e.g., Coco et al., 2007a, 2007b; Nienhuis et al., 2014; Dimas and Leftheriotis, 2019; Zgheib et al., 2018a, 2018b; Mazzuoli et al., 2019, 2020), field work (e.g., Traykovski et al., 1999; Nelson and Voulgaris,

2014; Wu and Parsons, 2019) and theoretical analysis (e.g., Blondeaux, 1990; Charru and Franklin, 2012). Ripples are generally classified into rolling-grain ripples and vortex ripples (Bagnold, 1946). Rolling-grain ripples form after the onset of sediment motion under low wave energy. Vortex ripples are taller features that produce flow separation and vortices over the downstream side of ripple crests, which maintain the ripple shape. A series of predictors has been developed to show that ripple dimensions are a function of wave orbital diameter, d_0 , defined as $d_0 = 2a_0 = H/\sinh(kh)$, where H is wave height, k is wave number, h is water depth and a_0 is the wave orbital amplitude (e.g., Miller and Komar, 1980; Wiberg and Harris, 1994; Traykovski et al., 1999; Goldstein et al., 2013). Alternative predictors show that ripple dimensions are dependent on the Shields parameter, θ (e.g., Nielsen, 1981; Grant and Madsen, 1982), the mobility number, ψ (e.g., Nielsen, 1981; Van Rijn, 1993; Mogridge et al., 1994; Styles and Glenn, 2002; Ruessink et al., 2015) or other non-dimensional parameters (e.g., Pedocchi and García, 2009). A number of other studies distinguish the orbital and anorbital ripples based on the ratio d_0/D_{50} (Wiberg and Harris, 1994). For a strong wave forcing $d_0/D_{50} > 5000$, equilibrium ripple spacing is proportional

* Corresponding author.

E-mail address: cjin987@aucklanduni.ac.nz (C. Jin).

to D_{50} and ripples are classified as anorbital ripples (Wiberg and Harris, 1994). When d_0/D_{50} is between 2000 and 5000, ripples are termed as sub-orbital ripples where the equilibrium ripple wavelength depends on both d_0 and D_{50} . When the ratio $d_0/D_{50} < 2000$, equilibrium ripple wavelength is proportional to d_0 and the often-quoted proportionality is 0.65 (Miller and Komar, 1980; Nienhuis et al., 2014; Pedocchi and García, 2009). This type of ripples is classified as orbital ripples which are the main focus in this study. Overall, ripple wavelength is associated with the vortex size generated on the lee side of ripples, and the length of the separation zone (e.g., Admiraal et al., 2006; Nienhuis et al., 2014).

When the wave forcing changes (i.e., wave height, wave period, or both), ripples do not adjust to the new equilibrium configuration instantaneously (e.g., Traykovski, 2007; Soulsby et al., 2012; Nelson and Voulgaris, 2014, 2015). The adjustment of ripples to the new wave conditions always lags behind the changes in wave forcing (hysteresis). Previous observational and laboratory work has focused on accounting for hysteresis in models of equilibrium ripple wavelength. Based on field observations, Traykovski et al. (1999) pointed out that ripple wavelengths are well predicted by a linear relationship with d_0 , but predictions become less accurate when rippled beds are adjusting. Doucette and O'Donoghue (2006) conducted laboratory experiments to evaluate ripple hysteresis under changes in wave forcing. They concluded that hysteresis is independent of initial bedform conditions, but depends on the mobility number, ψ , and the wave period, T , which can be expressed as

$$t_h = T \exp(-0.036\psi + 7.44) \quad (1)$$

where t_h is hysteresis time scale and T is wave period. The dependence of hysteresis on mobility number is also reported by Testik et al. (2005), but a different predictor is suggested:

$$t_h = \frac{C}{\omega\psi^2} \quad (2)$$

where $C = 2500$ is a constant and ω is wave frequency. Testik et al. (2005) also examined the threshold for sediment initiation and ripple formation over a pre-existing rippled bed (medium grain size of 0.4 mm). Sediment particles start moving at $\theta = 0.05$, but no ripples are able to form unless the maximum absolute value of Shields parameter is larger than 0.067. Smith and Sleath (2005) studied the variation of ripple height instead of ripple wavelength under the step-change in wave forcing. Ripple height grows or decays from the initial rippled bedforms in two stages, the initial and final stage. When the wave forcing increases, ripple height grows exponentially in both the initial and final stages, but in different growth rate. In terms of the decay process (decreasing in wave forcing), ripple height decreases linearly as a function of time in the initial stage and exponentially in the final stage. The transient time for the growth and decay from existing rippled bedforms depends on the ratio of the final and initial wave orbital diameter. Soulsby et al. (2012) proposed an alternative ripple predictor based on the data from Doucette and O'Donoghue (2006), where the time-evolving ripple wavelength adjusts exponentially to the change in wave conditions.

Previous work has examined morphological changes of bedform geometries during adjustment to a change in wave forcing. For example, a large decrease in wave amplitude results in ripple splitting (the emergence of secondary crests) and a decrease in the overall pattern spacing, usually termed as "doubling" (Hansen et al., 2001b; Sekiguchi and Sunamura, 2004; Nienhuis et al., 2014). This behavior is ascribed to the shorter wave orbital diameter, which reduces the sediment transport distance during each half-wave cycle, resulting in deposition between ripple crests and consequent formation of a secondary crest. Also, a slight change in wave forcing leads to "slides" of ripple crests to adjust to the new equilibrium geometry. Ripple crestlines become sinusoidal and distorted in the direction of wave propagation in response

to the increase of the wave forcing (a phenomenon termed as "bulging" by Hansen et al., 2001a, 2001b). Perron et al. (2018) categorized the response to changes in wave forcing according to the change in ripple spacing. If ripple spacing decreases by $\leq 35\%$ of the initial spacing, ripple crestlines distort and become "hourglass-shaped". For changes $\geq 35\%$, secondary crests form in the ripple troughs. Finally, the widening in ripple spacing can create a "zigzag" pattern where ripple crestlines are highly distorted and become almost sinusoidal.

As wave forcing changes, ripple morphology undergoes other types of readjustment and interactions, such as defect and bedform repulsion, merging, and lateral linking (Kocurek et al., 2010; Zgheib et al., 2018a). A defect is defined as an irregularity of a crestline. There are various types of defects: terminations, bifurcations, secondary crests and others. The term repulsion refers to defects merging with the downstream ripple crestline through migration and isolating the corresponding portion of the defects at the downstream ripple crestlines (for more details, see e.g., Zgheib et al., 2018a). Merging refers to a process that combines two separate crestlines into one, while lateral linking describes the process, usually occurring during the initial stages of ripple formation, when incipient crestlines connect to form one longer crestline. The deformation of a single ripple crest can alter hydrodynamics and sediment fluxes, over both the local ripple crest and around the neighboring area (Marieu et al., 2008; Kocurek et al., 2010; Zgheib et al., 2018a, 2018b). Zgheib et al. (2018a) developed a high-resolution numerical model to simulate bedform-defect interactions under unidirectional flow. The simulation results show the bedform interactions, for example, defect repulsion, bedform repulsion and merging. The occurrence of these interactions is all associated with the neighboring bedform structures. Physically, the upstream ripple geometries affect the hydrodynamics over downstream ripples and alter the downstream ripple migration speed and erosion-deposition patterns. Defect interactions (e.g., defect repulsion) also induce a cascade of repulsions affecting several crestlines downstream, showing that defects affect not only the local geometry, but well beyond into surrounding areas.

Although defect interactions have been addressed in previous studies (Werner and Kocurek, 1999; Marieu et al., 2008; Kocurek et al., 2010; Zgheib et al., 2018a; Myrow et al., 2018), it remains unclear how defect interactions and pre-existing bedform structures affect hysteresis. Existing prediction schemes relate ripple hysteresis purely to wave forcing. However, recent laboratory experiments and numerical simulations have shown that that pre-existing bedform morphology can significantly affect hysteresis (Marieu et al., 2008; Huntley et al., 2008; Jin et al., 2019). Marieu et al. (2008) developed a Reynolds-averaged Navier-Stokes (RANS) turbulence model evaluating the dependence of ripple development on the pre-existing rippled bedforms. The modeling results illustrate that the pre-existing bedform geometry has a strong influence on the adjustment rate to the final ripple wavelength. Huntley et al. (2008) pointed out that the defect density of pre-existing bedforms is a determining factor of hysteresis in a numerical model of bedform evolution. For example, a large defect density leads to faster adjustment (shorter hysteresis). Although the mechanism of ripple adjustment in the sediment sorting model of Huntley et al. (2008) is different from that leading to the adjustment of wave-generated ripples, it still highlights the importance of existing rippled bedforms on ripple adjustment. Perron et al. (2010) found support for his idea in laboratory wave tank experiments, noting that a higher density of defects allows a rippled bed to adjust more quickly to a change in wave conditions. Jin et al. (2019) evaluated the influence of existing wave-generated ripple patterns on hysteresis using laboratory experiments. Despite the limited number of experiments, the results suggest that defects on the pre-existing bedform affect ripple adjustment and possibly even control the final equilibrium ripple wavelength.

In this paper we examine factors contributing to the hysteresis time scale of vortex ripples to a change in wave conditions, and the role of defect density using data from the laboratory experiments of Perron et al. (2016, 2018) and Jin et al. (2019). The contribution of different factors

to ripple hysteresis is presented and discussed. We also show the interactions of two typical defects, and evaluate the influence of defects on ripple adjustment.

2. Methodology

We collected data from two experiments, Perron et al. (2016, 2018) (Exp. 1 hereafter) and Jin et al. (2019) (Exp. 2 hereafter), to investigate ripple hysteresis under sudden changes in wave forcing. Runs in Exp. 1 were conducted in a wave flume 7 m in length, 0.6 m in width and 0.5 m in depth, with a moto-driven paddle at one end to generate waves and an artificial beach at the opposite end to reduce wave reflection over a 5 cm-thick, well-sorted sand bed (median grain size $D_{50} = 0.18$ mm). In the first phase of each run in Exp. 1, ripples were generated from an initially flat bed, which was perturbed to accelerate ripple initiation, and allowed to evolve under a certain wave forcing until they reached a quasi-equilibrium state (Table 1). The wave height and period were then increased or decreased by adjusting the paddle stroke and the motor speed. Wave characteristics and water depth were recorded during each phase of the run. Bedform development was recorded using a camera deployed above the center of the wave flume. Time-lapse photos (Fig. 2a) were taken every 10–15 wave periods. We refer readers to Perron et al. (2016, 2018) for more details on the experimental settings.

Runs in Exp. 2 were conducted in a wave flume 54 m long and 2 m wide. The mobile sand test area is 18 m long at the center of the wave flume, with a thickness of 0.2 m, and median grain size of the well-sorted sand $D_{50} = 0.31$ mm. We performed runs with

an abrupt change in wave height to increase or decrease wave forcing. The initial wave conditions were the same for each paired run. However, we let the first phase of the run proceed for different durations before the abrupt change in wave forcing, which resulted in more defects (shorter phase 1) or fewer defects (longer phase 1) in different runs, since defects are generally eliminated over time during flow equilibration. This allowed for comparison of the influence of defect density on ripple hysteresis. The development of ripples was recorded using a camera deployed above the water surface. Photos were taken every 10 s (Fig. 2b). We refer readers to Jin et al. (2019) for more details on the experimental settings.

Basic calculated parameters of Exp. 1 and Exp. 2 are presented in Tables 1 and 2. More relevant parameters can be found in Appendix A. Wave orbital diameter, d_0 , and maximum velocity, U_m , were calculated using linear wave theory. The mobility number, ψ , was calculated as:

$$\psi = \frac{U_m^2}{((\rho_s - \rho)/\rho)gD_{50}} \tag{3}$$

where ρ_s and ρ are the density of sand and water, g is the acceleration of gravity. The maximum absolute value of Shields parameter (θ) is:

$$\theta = \frac{0.5f_w U_m^2}{((\rho_s - \rho)/\rho)gD_{50}} \tag{4}$$

Table 1

Conditions in Exp. 1. The subscripts 01 and 02 represent the parameters before and after the changes in wave conditions. T , H and U_m are wave period, wave height and maximum orbital velocity. ψ and θ are mobility number and Shields parameter. Δd_0 and $\Delta\theta$ are the change in wave orbital diameter and Shields parameter. t_h is the hysteresis. δ is the defect density. λ_{02} is the equilibrium ripple wavelength after the changes in wave conditions. $Re_{\delta z}$ is the Reynolds number based on Stokes boundary layer thickness.

| Run no. | T_{01} (s) | T_{02} (s) | H_{01} (m) | H_{02} (m) | U_{m01} (m/s) | U_{m02} (m/s) | d_{01} (m) | d_{02} (m) | Δd_0 (m) | ψ_{01} | ψ_{02} | θ_{01} | θ_{02} | $\Delta\theta$ | t_h (h) | δ (m^{-1}) | λ_{02} (m) | $Re_{\delta z}$ |
|---------|--------------|--------------|--------------|--------------|-----------------|-----------------|--------------|--------------|------------------|-------------|-------------|---------------|---------------|----------------|-----------|-----------------------|--------------------|-----------------|
| 110214 | 2.38 | 2.42 | 0.071 | 0.065 | 0.159 | 0.144 | 0.120 | 0.111 | -0.009 | 8.674 | 7.154 | 0.083 | 0.070 | -0.013 | 0.07 | 0.123 | 0.078 | 127 |
| 110215 | 1.79 | 2.31 | 0.049 | 0.070 | 0.104 | 0.155 | 0.059 | 0.114 | 0.055 | 3.685 | 8.226 | 0.048 | 0.080 | 0.033 | 1.517 | 0.408 | 0.078 | 133 |
| 110216 | 3.22 | 2.40 | 0.055 | 0.064 | 0.131 | 0.144 | 0.135 | 0.110 | -0.025 | 5.921 | 7.097 | 0.054 | 0.070 | 0.017 | 1.300 | 0.434 | 0.073 | 126 |
| 110217 | 3.14 | 2.33 | 0.054 | 0.065 | 0.129 | 0.145 | 0.128 | 0.108 | -0.020 | 5.669 | 7.228 | 0.053 | 0.072 | 0.019 | 1.650 | 0.093 | 0.076 | 125 |
| 110225 | 1.92 | 2.08 | 0.060 | 0.073 | 0.131 | 0.162 | 0.080 | 0.107 | 0.027 | 5.850 | 9.004 | 0.066 | 0.090 | 0.024 | 2.130 | 0.676 | 0.071 | 131 |
| 110226 | 2.53 | 2.05 | 0.068 | 0.074 | 0.156 | 0.164 | 0.126 | 0.107 | -0.019 | 8.383 | 9.207 | 0.078 | 0.092 | 0.014 | 0.267 | 0.703 | 0.071 | 132 |
| 110227 | 2.34 | 2.64 | 0.062 | 0.058 | 0.137 | 0.132 | 0.102 | 0.111 | 0.009 | 6.410 | 5.986 | 0.066 | 0.059 | -0.007 | 2.983 | 0.262 | 0.078 | 121 |
| 110228 | 2.61 | 2.61 | 0.078 | 0.058 | 0.174 | 0.130 | 0.144 | 0.108 | -0.036 | 10.404 | 5.784 | 0.092 | 0.058 | -0.035 | 3.200 | 0.805 | 0.074 | 119 |
| 110301 | 3.15 | 2.60 | 0.074 | 0.059 | 0.171 | 0.133 | 0.170 | 0.110 | -0.060 | 10.017 | 6.071 | 0.084 | 0.060 | -0.024 | 1.767 | 0.899 | 0.076 | 121 |
| 110302 | 2.88 | 2.09 | 0.070 | 0.077 | 0.160 | 0.165 | 0.146 | 0.110 | -0.036 | 8.741 | 9.377 | 0.078 | 0.092 | 0.015 | 1.017 | 0.246 | 0.074 | 135 |
| 110303 | 1.83 | 2.01 | 0.060 | 0.079 | 0.122 | 0.167 | 0.071 | 0.106 | 0.035 | 5.088 | 9.534 | 0.060 | 0.096 | 0.035 | 1.717 | 0.435 | 0.074 | 133 |
| 110308 | 2.14 | 2.12 | 0.054 | 0.073 | 0.115 | 0.157 | 0.078 | 0.106 | 0.028 | 4.554 | 8.504 | 0.052 | 0.085 | 0.033 | 1.117 | 0.604 | 0.073 | 129 |
| 110309 | 2.12 | 2.11 | 0.064 | 0.074 | 0.136 | 0.159 | 0.092 | 0.107 | 0.015 | 6.378 | 8.700 | 0.067 | 0.087 | 0.019 | 0.073 | 0.491 | 0.074 | 130 |
| 110310 | 2.76 | 3.05 | 0.061 | 0.048 | 0.138 | 0.110 | 0.121 | 0.107 | -0.014 | 6.501 | 4.176 | 0.062 | 0.041 | -0.021 | NA | 0.389 | N/A | 108 |
| 110314 | 3.25 | 3.11 | 0.068 | 0.048 | 0.156 | 0.109 | 0.055 | 0.108 | 0.053 | 8.322 | 4.082 | 0.111 | 0.041 | -0.070 | NA | 0.364 | N/A | 109 |
| 110315 | 3.14 | 3.08 | 0.059 | 0.047 | 0.134 | 0.106 | 0.134 | 0.105 | -0.029 | 6.187 | 3.890 | 0.056 | 0.039 | -0.018 | NA | 0.331 | N/A | 105 |
| 110316 | 3.08 | 3.09 | 0.056 | 0.047 | 0.129 | 0.109 | 0.126 | 0.107 | -0.019 | 5.681 | 4.048 | 0.053 | 0.041 | -0.013 | NA | 0.419 | N/A | 108 |
| 110317 | 2.12 | 3.12 | 0.055 | 0.045 | 0.117 | 0.105 | 0.079 | 0.104 | 0.025 | 4.731 | 3.774 | 0.053 | 0.038 | -0.015 | NA | 0.260 | N/A | 105 |
| 110503 | 2.93 | 3.15 | 0.061 | 0.047 | 0.141 | 0.110 | 0.131 | 0.110 | -0.021 | 6.814 | 4.130 | 0.063 | 0.041 | -0.022 | NA | 0.000 | N/A | 110 |
| 110504 | 1.98 | 2.74 | 0.048 | 0.055 | 0.100 | 0.125 | 0.063 | 0.109 | 0.046 | 3.421 | 5.346 | 0.043 | 0.053 | 0.010 | 4.250 | 0.842 | 0.077 | 117 |
| 110506 | 3.18 | 3.11 | 0.071 | 0.049 | 0.165 | 0.112 | 0.167 | 0.111 | -0.056 | 9.330 | 4.331 | 0.079 | 0.042 | -0.036 | NA | 0.497 | N/A | 111 |
| 110507 | 2.23 | 2.24 | 0.051 | 0.069 | 0.113 | 0.154 | 0.080 | 0.110 | 0.030 | 4.381 | 8.172 | 0.049 | 0.080 | 0.031 | 1.479 | 0.480 | 0.071 | 130 |
| 110508 | 3.47 | 2.70 | 0.058 | 0.054 | 0.138 | 0.124 | 0.152 | 0.106 | -0.046 | 6.534 | 5.250 | 0.057 | 0.053 | -0.004 | 1.888 | 0.422 | 0.072 | 115 |
| 110510 | 2.79 | 2.49 | 0.043 | 0.059 | 0.099 | 0.135 | 0.088 | 0.107 | 0.019 | 3.368 | 6.226 | 0.036 | 0.062 | 0.026 | 2.407 | 0.628 | 0.074 | 120 |
| 110511 | 3.12 | 2.85 | 0.057 | 0.051 | 0.132 | 0.119 | 0.131 | 0.108 | -0.023 | 6.007 | 4.852 | 0.055 | 0.048 | -0.007 | 14.73 | 0.579 | N/A | 113 |
| 110512 | 2.97 | 2.82 | 0.058 | 0.052 | 0.136 | 0.122 | 0.128 | 0.109 | -0.019 | 6.347 | 5.075 | 0.059 | 0.051 | -0.008 | 0.403 | 0.307 | 0.081 | 116 |
| 110515 | 3.36 | 2.85 | 0.075 | 0.052 | 0.175 | 0.119 | 0.188 | 0.108 | -0.080 | 10.557 | 4.873 | 0.085 | 0.048 | -0.036 | 5.330 | 1.711 | 0.080 | 113 |
| 110516 | 1.91 | 3.00 | 0.058 | 0.049 | 0.123 | 0.114 | 0.074 | 0.109 | 0.035 | 5.160 | 4.448 | 0.060 | 0.044 | -0.016 | 5.785 | 0.079 | 0.076 | 111 |
| 110517 | 2.63 | 2.89 | 0.046 | 0.050 | 0.106 | 0.117 | 0.088 | 0.107 | 0.019 | 3.839 | 4.672 | 0.042 | 0.047 | 0.005 | 2.313 | 0.187 | 0.075 | 112 |
| 110518 | 3.49 | 2.69 | 0.062 | 0.055 | 0.147 | 0.126 | 0.163 | 0.108 | -0.055 | 7.428 | 5.484 | 0.063 | 0.054 | -0.009 | 5.047 | 0.513 | 0.080 | 117 |
| 120303 | 3.23 | 1.60 | 0.060 | 0.055 | 0.142 | 0.11 | 0.146 | 0.056 | -0.090 | 6.901 | 4.152 | 0.061 | 0.055 | -0.007 | 4.914 | 0.646 | 0.052 | 79 |
| 120308 | 2.38 | 1.58 | 0.057 | 0.057 | 0.134 | 0.112 | 0.121 | 0.056 | -0.065 | 6.168 | 4.295 | 0.059 | 0.057 | -0.002 | 5.658 | 0.798 | 0.047 | 79 |
| 120312 | 2.73 | 1.61 | 0.069 | 0.056 | 0.157 | 0.109 | 0.136 | 0.056 | -0.080 | 8.409 | 4.108 | 0.077 | 0.054 | -0.023 | 2.990 | 1.117 | 0.047 | 78 |
| 120314 | 1.69 | 2.83 | 0.053 | 0.056 | 0.108 | 0.131 | 0.058 | 0.118 | 0.060 | 3.980 | 5.863 | 0.052 | 0.057 | 0.005 | 5.635 | 1.026 | 0.107 | 124 |
| 120316 | 1.63 | 2.89 | 0.056 | 0.055 | 0.112 | 0.129 | 0.058 | 0.118 | 0.060 | 4.291 | 5.690 | 0.056 | 0.055 | -0.001 | 6.944 | 1.055 | 0.090 | 124 |
| 120320 | 1.53 | 2.76 | 0.057 | 0.057 | 0.110 | 0.133 | 0.053 | 0.117 | 0.064 | 4.138 | 6.072 | 0.056 | 0.058 | 0.002 | 6.386 | 0.287 | 0.089 | 125 |

Table 2
Conditions in Exp. 2. The symbols are the same as in Table 1.

| Run no. | T_{01} (s) | T_{02} (s) | H_{01} (m) | H_{02} (m) | U_{m01} (m/s) | U_{m02} (m/s) | d_{01} (m) | d_{02} (m) | Δd_0 (m) | ψ_{01} | ψ_{01} | θ_{01} | θ_{02} | $\Delta\theta$ | t_h (h) | δ (m^{-1}) | λ_{02} (m) | $Re_{\delta 2}$ |
|---------|--------------|--------------|--------------|--------------|-----------------|-----------------|--------------|--------------|------------------|-------------|-------------|---------------|---------------|----------------|-----------|-----------------------|--------------------|-----------------|
| Exp2-1 | 2.5 | 2.5 | 0.12 | 0.09 | 0.271 | 0.204 | 0.216 | 0.162 | -0.054 | 14.693 | 8.265 | 0.138 | 0.087 | -0.051 | 0.32 | 0.46 | 0.1025 | 181 |
| Exp2-2 | 2.5 | 2.5 | 0.12 | 0.09 | 0.271 | 0.204 | 0.216 | 0.162 | -0.054 | 14.693 | 8.265 | 0.138 | 0.087 | -0.051 | 0.19 | 0.69 | 0.1059 | 181 |
| Exp2-3 | 2.5 | 2.5 | 0.15 | 0.09 | 0.339 | 0.204 | 0.270 | 0.162 | -0.108 | 22.958 | 8.265 | 0.198 | 0.087 | -0.111 | 0.31 | 1.17 | 0.1048 | 181 |
| Exp2-4 | 2.5 | 2.5 | 0.12 | 0.15 | 0.271 | 0.339 | 0.216 | 0.270 | 0.054 | 14.693 | 22.958 | 0.138 | 0.198 | 0.060 | 0.13 | 0.09 | 0.1329 | 302 |
| Exp2-5 | 2.5 | 2.5 | 0.09 | 0.15 | 0.204 | 0.339 | 0.162 | 0.270 | 0.108 | 8.265 | 22.958 | 0.087 | 0.198 | 0.111 | 0.11 | 0.13 | 0.1364 | 302 |
| Exp2-6 | 2.5 | 2.5 | 0.12 | 0.15 | 0.271 | 0.339 | 0.216 | 0.270 | 0.054 | 14.693 | 22.958 | 0.138 | 0.198 | 0.060 | 0.02 | 0.91 | 0.1342 | 302 |

where f_w is the wave friction factor (Swart, 1974)

$$f_w = \begin{cases} \exp \left[5.213 \left(\frac{k_s}{a_0} \right)^{0.194} - 5.977 \right] & \text{for } \frac{a_0}{k_s} > 1.57 \\ 0.3 & \text{for } \frac{a_0}{k_s} \leq 1.57 \end{cases} \quad (5)$$

$k_s = 2.5D_{50}$ is the hydraulic roughness, and a_0 is the wave orbital amplitude. The parameters d_0 and θ in both the initial stage and the second stage of the experiments are given (Fig. 2). d_{01} and d_{02} are wave orbital diameters before and after the changes in wave forcing, respectively. θ_{01} and θ_{02} are the maximum absolute value of Shields parameters (the Shields parameter mentioned hereafter refers to the maximum absolute value of Shields parameter) before and after the change in wave forcing. d_{02} is ~ 0.11 m for the majority of runs in Exp. 1. Notably, there are three exceptions where d_0 was shortened to around 0.058 m. The change in wave orbital diameter (Δd_0) ranged from 0.009 m to 0.065 m (Fig. 1a). The maximum absolute value of Shields parameter was lower than 0.12 for all cases in Exp. 1 (Fig. 1b). In Exp. 2, wave period was fixed at 2.5 s, and three different wave heights (0.09 m, 0.12 m and 0.15 m) were applied. The initial and final wave orbital diameters ranged from 0.162 m to 0.27 m, which were relatively larger than those in Exp. 1. Shields parameter in Exp. 2 ranged from 0.087 to 0.198. The Reynolds number base on Stokes boundary layer thickness is calculated for all cases and listed in Tables 1 and 2. It is defined as:

$$Re_{\delta} = \frac{U_m \delta_b}{\nu} \quad (6)$$

where $\delta_b = \sqrt{2\nu/\omega}$ is the Stokes boundary layer thickness, ν is kinematic viscosity and $\omega = 2\pi/T$ is the angular frequency. Ripple wavelength is derived from the spectrum of time-lapse photos taken during both experiments (Perron et al., 2018; Jin et al., 2019). In line with

previous studies, hysteresis is determined as the time elapsed from the change in wave forcing to the time when bedforms reach a new equilibrium geometry (Jin et al., 2019). In line with Jin et al. (2019), we consider the average ripple wavelength within the last hour of the runs as the equilibrium wavelength (assuming wave conditions are constant). Finally, we applied the definition of defect density, δ , the number of defects per overall length of ripple crestlines, from Werner and Kocurek (1999), to quantify the irregularity of the bedforms before the changes in wave conditions. Defect density is calculated as:

$$\delta = \frac{N}{L_c} \quad (7)$$

where N is the number of defects and L_c is the overall length of ripple crestlines. The number of defects is counted manually from the last image before the change in wave conditions. The crestlines are detected using the algorithm presented by Skarke and Trembanis (2011) based on fingerprint analysis. We provided photographic examples of different defect densities (Fig. 2).

3. Results and discussion

3.1. Dependence of the hysteresis time scale on wave orbital diameter and mobility number

We examined the dependence of hysteresis on the magnitude of d_{02} (Fig. 3), and in all runs in both experiments, there are changes in d_0 ($\Delta d_0 \neq 0$). Δd_0 is an overall control on hysteresis; if $\Delta d_0 = 0$, there is no change in equilibrium ripple wavelength, and by definition no hysteresis. As mentioned, d_{02} is approximately 0.11 m for the majority of runs in Exp. 1, but the same d_{02} does not result in identical hysteresis (t_h varied from 0.07 to 7 h for $d_{02} \approx 0.11$ m). For the three cases with lower d_{02} in Exp. 1 ($d_{02} \approx 0.058$ m), the magnitude of the response time was

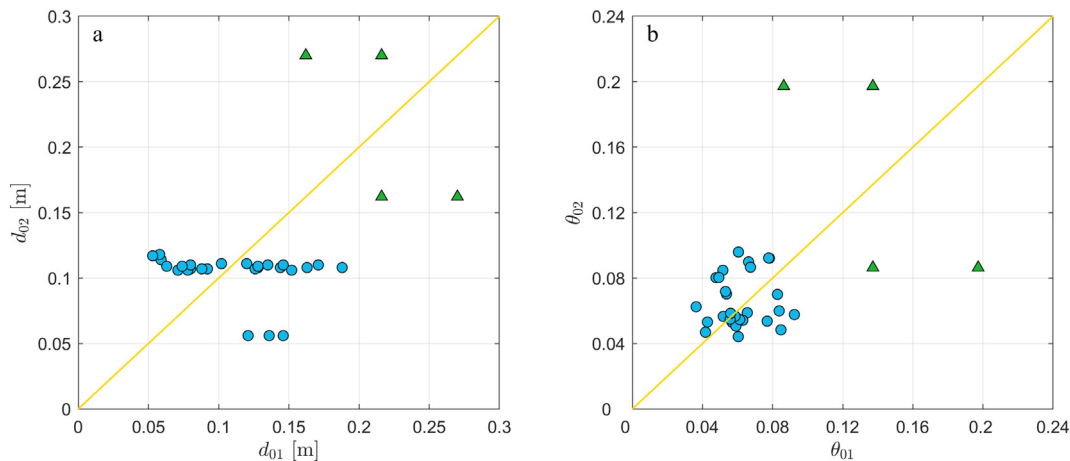


Fig. 1. Wave orbital diameter d_0 (a) and Shields parameter θ_0 (b) before (d_{01} , θ_{01}) and after (d_{02} , θ_{02}) the change in wave conditions. Blue filled circles represent the runs from Perron et al. (2018) and the green filled triangles represent the runs from Jin et al. (2019). The yellow line indicates no change in wave orbital diameter (a) or Shields parameter (b).

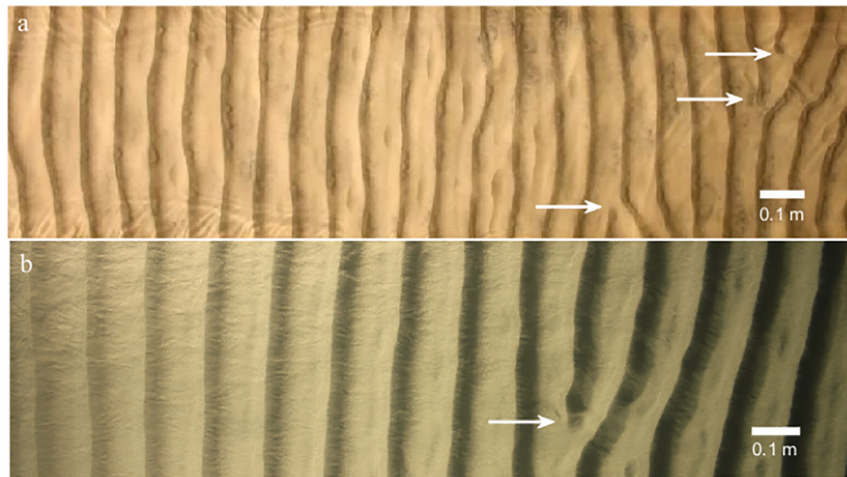


Fig. 2. Photos taken by cameras above the wave flume in (a) Exp. 1 with three crest terminations and (b) Exp. 2 with one crest termination. The termination defects are highlighted with the white arrows.

generally longer, and it also varied between cases ($t_h = 3\text{--}6$ h). We also observed different t_h for the same d_{02} in runs with different Δd_0 in Exp. 2. Overall, despite the large variability, there was a decreasing trend of hysteresis with increasing d_{02} under the condition Δd_0 not equal to 0.

The magnitude of Δd_0 results in radically different hysteresis time scale (Fig. 5), even in those cases in which d_{02} is approximately the same and thus the end result is nearly identical equilibrium ripple wavelength (Fig. 4a; $t_h = 1.3$ h versus $t_h = 3.2$ h) (Fig. 5; all cases with $d_{02} \approx 0.11$ m). Negative Δd_0 represents a decrease (shortening) in wave orbital diameter, and positive Δd_0 represents an increase (lengthening) of the wave orbital diameter (Fig. 5). Larger changes in wave orbital diameter result in greater hysteresis, particularly if the wave orbital diameter is lengthened. The proportionality constant (k) relating hysteresis to the changes in wave orbital diameter varies between -57 h/m for negative Δd_0 and 88 h/m for positive Δd_0 .

Despite the large variability, our study indicates that d_{02} could also account for the general trend of ripple hysteresis. Our observation that d_{02} is a dominant factor controlling the hysteresis is consistent with the hypothesis of Jin et al. (2019) when Δd_0 is not equal to 0. Although the experiments investigated here do not cover a wide range of wave

orbital diameters, the contribution of the change in wave orbital diameter to the ripple adjustment time is evident. We hypothesize that the control of Δd_0 on hysteresis might be due to the different amount of sediment transport necessary to achieve the new equilibrium configurations when wave conditions change more or less drastically.

The mobility number has previously been used to describe ripple hysteresis (Doucette and O'Donoghue, 2006; Testik et al., 2005), and our data are in agreement with this conclusion (Fig. 6). To compare our results with the existing model, we normalized hysteresis to the wave period. This results in a decrease in normalized hysteresis with the increase of the mobility number, and the relationship can be quantified as $t_h = T_{02} \exp(-0.399M_{02} + 10.72)$. The predictor from Doucette and O'Donoghue (2006) provides a reasonable estimation of hysteresis, but the ripple adjustment rate from Doucette and O'Donoghue (2006) is slightly slower than the predictor developed here.

Although the mobility number gives a reasonable prediction of the normalized hysteresis, it does not fully explain the variability in hysteresis in our experiments. For instance, in runs 110503 and 120303 (Fig. 4b), the initial and final mobility numbers are almost the same (6.8 before and 4.1 after the change in wave conditions in run 110503 compared to 6.9 before and 4.2 after in run 120303), yet ripple wavelength decreased rapidly in run 120303 after wave conditions changed but did not change detectably in run 110503. These different responses could be due to differences in the initial and final wave orbital diameters, equilibrium ripple wavelengths and different Shields parameters in each run. The mobility number in our experiments is always smaller than 25, implying that bedload dominates sediment transport (Dimas and Leftheriotis, 2019). Because wave orbital diameter, Shields parameter, ripple height and other parameters that vary in our experiments undoubtedly affect bedload transport, they should also influence the hysteresis.

3.2. Threshold value of the Shields parameter for ripple readjustment

As previously indicated, in Exp. 1 not all ripples evolve towards new equilibrium wavelengths after the change in wave conditions – we highlight two cases (Fig. 7) in which we use the predictor of Goldstein et al. (2013). In both cases, ripple wavelengths appear to have almost reached an equilibrium wavelength before the change in wave conditions and the wavelength is well predicted by the model of Goldstein et al. (2013). After the change in wave conditions, ripples in both experiments adjust at an extremely slow rate or do not readjust at all (the hysteresis is much longer than the duration of the experiment). We

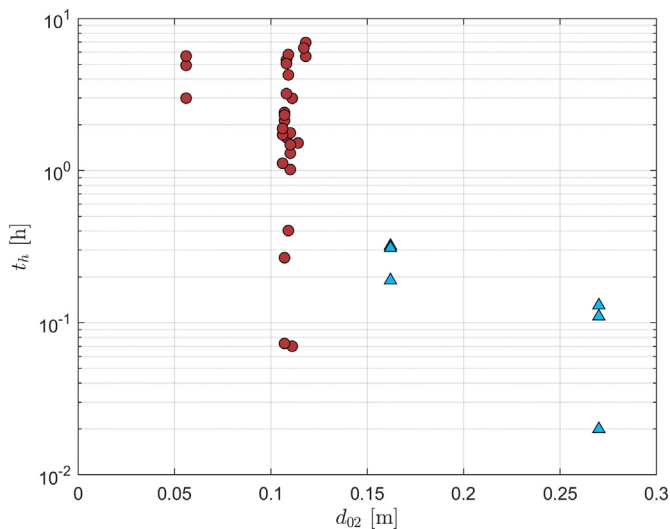


Fig. 3. Hysteresis (t_h) as a function of d_{02} . Circles represent data from Exp. 1 and triangles represent data from Exp. 2.

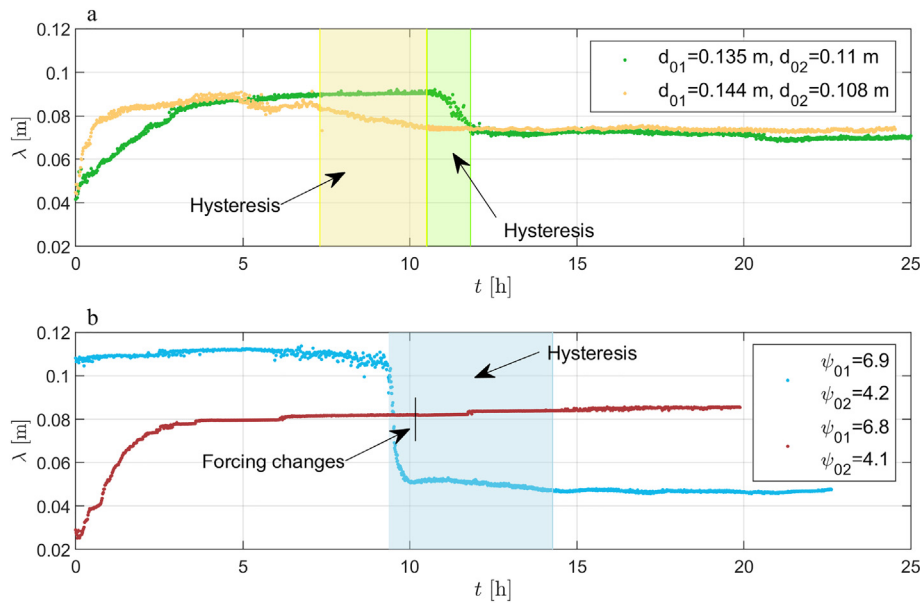


Fig. 4. Time-evolving ripple wavelength for runs 110216 (a, green dots), 110228 (a, yellow dots), 110503 (b, red dots) and 120303 (b, blue dots) in Exp. 1. (a) Wave orbital diameter and (b) mobility number before and after the change in wave conditions are shown in the legend. Hysteresis is highlighted using the same colors as above for each run. There is no detectable change in ripple wavelength for run 110503 (red dots) after the decrease in mobility number (denoted by the black line).

are unable to quantify the hysteresis for these cases (hysteresis is indicated with NA in Table 1).

We examined the relation between the Shields parameter and normalized hysteresis for all runs (Fig. 8a), including those where we are unable to quantify hysteresis. In runs terminated before the bed equilibrated to the new wave conditions, we plotted the time between the change in wave conditions and the end of runs instead. We acknowledge that the actual hysteresis is much longer than plotted for these runs and that, in some cases, equilibrium might never be reached. In run 110511, ripple spacing changes almost continuously but does not reach the equilibrium ripple wavelength at the end of the experiment.

In the aforementioned runs, sediment transport occurs until the end of the run (observed in the collected images) even though the Shields parameters at the end of these runs are, in some cases, lower than the critical Shields parameter (0.051) for sediment motion from a flat bed with $D_{50} = 0.18$ mm (Soulsby and Whitehouse, 1997). Given that ripple adjustment is still occurring after the change in wave conditions in run 110516 ($\theta_{02} = 0.044$), but not run 110506 ($\theta_{02} = 0.042$), we suggest that the effective bulk threshold of ripple adjustment from the pre-existing ripple geometry for $D_{50} = 0.18$ mm must be ~ 0.043 , and thus even lower than the threshold for sediment motion from a flat bed. The velocity over ripple crest can be 1.5–2 times free stream velocity

(Van der Werf et al., 2007; Fredsøe et al., 1999; Önder and Yuan, 2019) and induce high shear stress over ripple crests capable of moving sediment particles. This might explain the sediment motion we observed at Shields parameters below the threshold for sediment motion from a flat bed. This threshold of the Shields parameter explains the lack of adjustment in ripple geometry for run 110503 (Fig. 4b; $\theta_{02} = 0.041$).

A Shields parameter of 0.043 can be considered as the threshold for ripple adjustment in these experiments with $D_{50} = 0.18$ mm (Fig. 8a). The ratio ψ/Re_δ plays an important role in controlling sediment-flow interactions when turbulence is not triggered (Mazzuoli et al., 2019, 2020). The dependence of the hysteresis on ψ/Re_δ includes an evident threshold for ripple readjustment in response to the change in wave conditions (Fig. 8b). This might indicate that below the threshold, sediment transport is too small to affect the ripple geometry. However, there is one exception (“A”, Fig. 8a). The temporal variation of the ripple wavelength for this case is shown in Fig. 9. The sign of change in wave period and height in this run (increase in wave period, decrease in wave height) differs from any other run. This results in an increase of the wave orbital diameter from 0.079 m to 0.104 m, but a decrease in the Shields parameter. θ_{01} (0.053) exceeds the apparent threshold sediment motion from the rippled bed, but θ_{02} (0.038) is lower than the

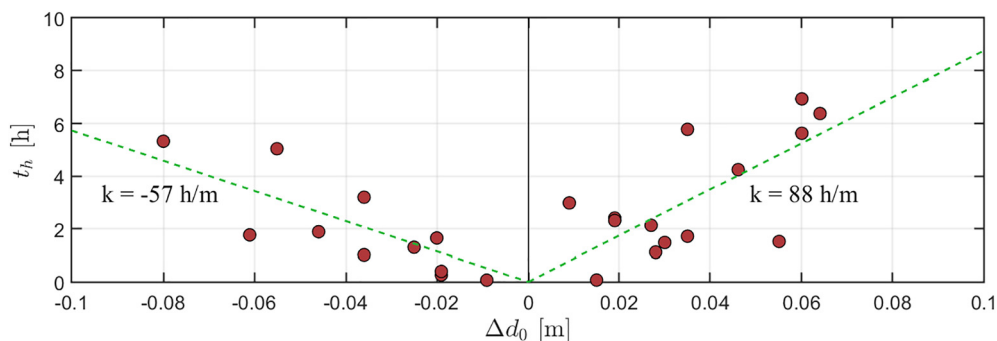


Fig. 5. The dependence of non-dimensional hysteresis (t_h/T_{02}) on the changes in wave orbital diameter (Δd_0). The dark red dots represent the runs from Exp. 1. The green dashed lines are trend lines passing through the origin for both decrease and increase of the wave orbital diameter.

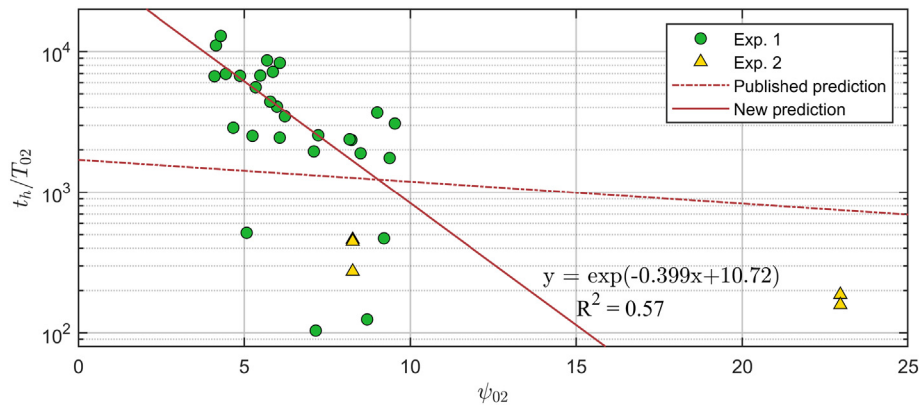


Fig. 6. Dependence of non-dimensional hysteresis (t_h/T) on mobility number. Green circles are from Exp. 1 and yellow triangles are from Exp. 2. The red dash-dotted line shows the prediction from Doucette and O'Donoghue, 2006. The solid line is the regression model generated with the data from Exp. 1 and Exp. 2. The equation and R^2 refer to the solid line.

threshold. In this case, we would theoretically expect ripples to develop before but not after the change in wave conditions. However, surprisingly, observation is the opposite of our expectation. We observe that only a few ripples developed from the initial perturbed bed for the initial 7 h (Fig. 9c, d), but when the Shields parameter was decreased to 0.038 (as a result of an increase of the wave period and decrease in wave height), rapid ripple formation occurred (Fig. 9e, f). There are two possible explanations. (1) The critical Shields parameter for ripple formation is strongly affected by the presence of pre-existing bedforms. It has already been suggested that the threshold for sediment motion is highly reduced with the presence of ripples and the threshold is related to the dimensions of ripples (e.g., Green and Black, 1999). We here hypothesize that the threshold for ripple readjustment is also related to the bedform characteristics and resulting flow dynamics. (2) The threshold for ripple readjustment depends on other factors that differ in some unique way for this run, for example, wave orbital diameter or changes in wave period.

According to previous studies, the critical Shields parameter for the initiation of sediment motion for $D_{50} = 0.18$ mm is around 0.051 (Soulsby and Whitehouse, 1997). The critical shear velocity for ripple readjustment is 1.16 times that for sediment motion

(Testik et al., 2005). Accordingly, the threshold for ripple readjustment is 0.068 for $D_{50} = 0.18$ mm. In this study, the initial bedforms in Exp. 1 are perturbed to accelerate ripple development. Thus, the initial surface is not flat. For experiments 110215, 110504, 110510 and 110517 (Table 1), the initial Shields parameter is ≤ 0.051 , but sediment is set into motion from the start of experiments (see the corresponding movies in Perron et al., 2016). This might be ascribed as the turbulence induced by the uneven bedforms (Jerolmack and Mohrig, 2005; Mazzuoli et al., 2018), which enables sediment transport for Shields parameter below 0.051. The initial bedforms seem to accelerate the development rate of ripples after perturbation of the flow, which reduces the critical Shields number for sediment initiation. Another possible reason we can think about is that the calculation from the linear wave theory are not quite a perfect description of actual conditions in the flume.

Our results indicate that pre-existing bedforms are difficult to alter if the Shields parameter is lower than 0.043 in Exp. 1 ($D_{50} = 0.18$ mm), even if there is sediment transport. This is consistent with Testik et al. (2005) who show that the threshold of sediment motion is lower than that for ripple readjustment; the one difference is that our study reports lower threshold values.

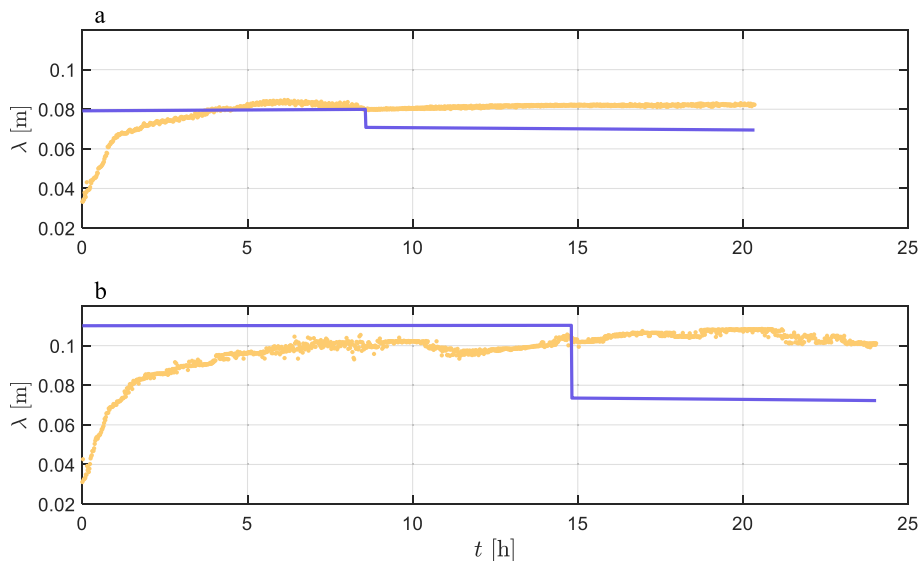


Fig. 7. Temporal evolution of ripple wavelength (yellow dots) for runs where ripples did not reach equilibrium after changes in wave conditions (Exp. 1). Two examples are shown: (a) 110310 and (b) 110506. Blue lines are the prediction of ripple wavelength from Goldstein et al. (2013).

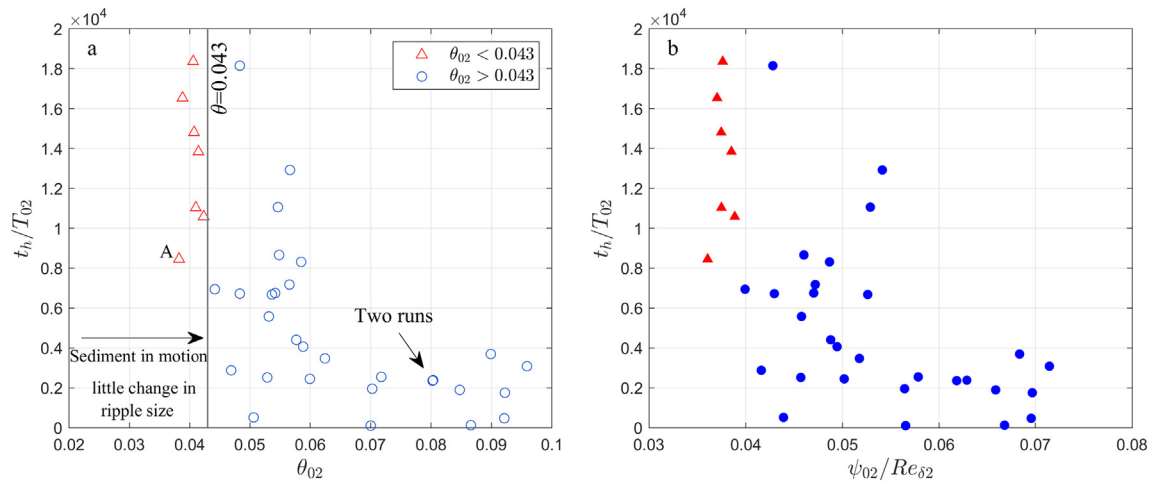


Fig. 8. (a) Relation between normalized hysteresis (t_h/T_{02}) and Shields parameter (θ_{02}). Circles represent the runs with the bedforms reaching equilibrium before the end of the experiment except the run 110511 with $\theta_{02} = 0.048$ and $t_h/T_{02} = 1.81 \times 10^4$ (although equilibrium is not reached at the end of the run, we observe a continuous change in ripple wavelength after the change in wave conditions). Triangles represent runs with no change in ripple wavelength (or extremely slow changes in ripple wavelength) after the change in wave conditions. The gray line shows the apparent threshold Shields parameter ($\theta_{02} = 0.043$). The temporal variation of ripple wavelength for case A is plotted in Fig. 9. (b) The dependence of t_h/T_{02} on ψ_{02}/Re_{δ_2} . Red filled triangles represent runs with little adjustment in ripple wavelength after the change in wave conditions. Blue filled circles represent runs with adjustment in ripple wavelength after the change in wave conditions.

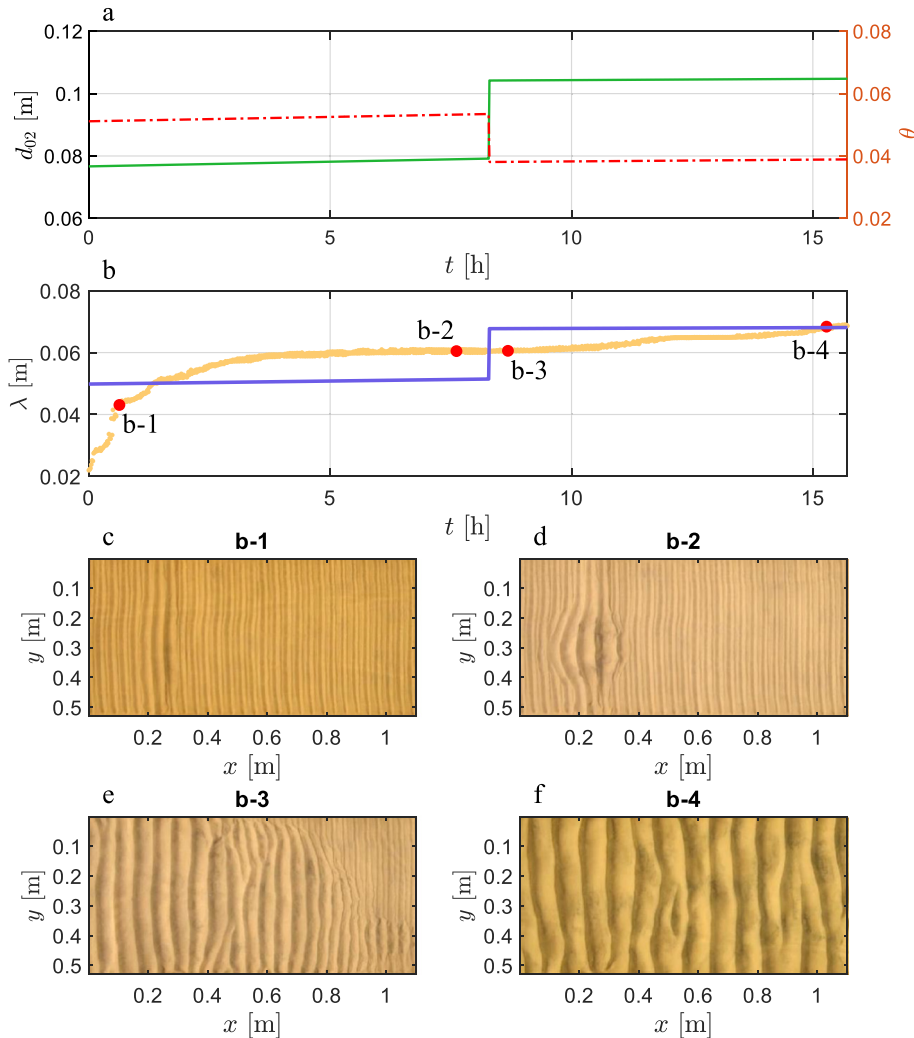


Fig. 9. Time series of (a) wave orbital diameter (d_{01} and d_{02} ; green line), Shields parameter (red dash-dot line), and (b) ripple wavelength showing the moment images (c–f) were taken (b-1, b-2, b-3, b-4) during ripple growth in run 110317. (b) also shows temporal variation of ripple wavelength (yellow dots) and the prediction ($0.65d_0$, blue line) by Wiberg and Harris (1994). Notice that the pattern visible at the moment b-1 (c) and most patterns visible at the moment b-2 (d) are grooves. The patterns at the upper right corner at the moment b-3 (e) are rakes. They are not ripples.

3.3. Effects of defect density and defect interactions on bedform evolution

We examine the influence of defect density on hysteresis (Fig. 10). We focus on examining paired cases — those with almost the same θ_{01} and θ_{02} but with different defect densities. We have three paired runs (110214 and 110217, 110215, 110308 and 110507, 110226 and 110302) selected from the experiments with an increase of the Shields parameter in Exp. 1. One pair of runs (Exp2-4 and Exp2-6) with an increase of the Shields parameter is selected as a comparison from Exp. 2. A larger defect density resulted in shorter hysteresis in all these paired cases. The extent to which defect shortens hysteresis varies with the Shields parameter. For a high Shields parameter, greater defect density causes a small absolute (though fractionally larger) decrease in hysteresis. As the Shields parameter increases from 0.07 to 0.2, the fractional extent to which the response time shortens (difference of the hysteresis between paired runs divided by the hysteresis of the run with lower defect density) increases from 21% for $\theta_{02} = 0.07$ to 85% for $\theta_{02} = 0.2$.

When the pre-existing ripple geometry is subject to a change in wave conditions that lengthens the orbital diameter, defects always interact with each other to generate a wider ripple spacing. Greater defect density in eolian bedforms was shown to promote lateral linking, merging and repulsion (Werner and Kocurek, 1997; Kocurek et al., 2010). As a result, we hypothesized that greater defect density could result in faster wave ripple adjustment. Our results bear this out and are consistent with the modeling results of Huntley et al. (2008), although defect density does not affect hysteresis as strongly in our experiments as presented in Huntley et al. (2008).

Pre-existing bedform characteristics exhibit defect interactions when the wave forcing undergoes significant changes (e.g., Werner and Kocurek, 1997, 1999). Time-lapse photos reveal that, under certain conditions, defect interaction helps accommodate changes in ripple spacing (Werner and Kocurek, 1999). For instance, we tracked a series of eye defects from their formation to disappearance using time-lapse photos. Eye defects (which Perron et al. (2018) referred to as “cups”) are a short-lived defect in our experiments. They are different from terminations and bifurcations, which can exist during the entire process of ripple adjustment (Perron et al., 2018). Eye defects are formed by the migration of a small short secondary crestline (Fig. 11a-1, yellow arrows), when only part of the short small secondary crest migrates and

connects with a longer crestline to form the eye defect. Three types of interactions occur (Fig. 11). A common interaction occurs when a short secondary crestline and a termination exist on the either side of a long continuous crestline (Fig. 11a). The growth of the small secondary crest gradually distorts the long continuous crestlines. Then the small secondary crest connects with the long crestline (Fig. 11a-3) and a part of the crestline that belongs to the original long crestline detaches (Fig. 11a-4). These processes are also termed “bedform repulsion” (e.g., Kocurek et al., 2010; Zgheib et al., 2018a). The crestlines that have detached are subsequently connected with the termination on the side of the long crestline, forming a continuous ripple crestline (Fig. 11a-5 and a-6).

Eye defect can also decay (Fig. 11b). The size of eye defects decreases as the ripple crestlines gradually connect with each other, but the cause of this is still unclear. After the disappearance of eye defects, a small amount of sediment accumulates on both sides of the crestline. In addition, eye defects can form in the absence of termination defects from the interaction between defects and ripples (Fig. 11c). A short small crestline may migrate and connect with a longer ripple crestline downstream (Fig. 11c-2). This interaction results in the migration of another small secondary crest, forming an eye defect (Fig. 11c-4, yellow arrow). After the interactions, the small secondary crest is connected with the long crestline (Fig. 11c-1, yellow arrow), but a new small secondary crestline forms downstream.

Terminations show some common behaviors (Fig. 12a), including the interactions of terminations when termination defects exist on both sides of a distorted long crestline, and when two termination defects face the opposite directions (Fig. 12a-1). As the migration of terminations towards each other, the crestline between the two terminations becomes more distorted (Fig. 12a-2). The distorted crestline then splits and links with the two terminations (Fig. 12a-3). Finally, the terminations disappear and two continuous crestlines are generated (Fig. 12a-4 and a-5). When two terminations face each other (Fig. 12b-1), they migrate towards each other until they link together forming a continuous crestline (Fig. 12b). Interactions between terminations and bedforms also occurs when there are two, long, distorted crestlines in between (Fig. 12c-1). The mechanism of the interactions is similar that just discussed (Fig. 12a). The distorted crestlines connect with the terminations on the two sides forming continuous crestlines. The difference between the two cases is the numbers of long distorted crestlines between two terminations. The interactions result in three continuous crestlines rather than two (Fig. 12a).

We further evaluate the variation of the spectra when defect interactions occur (Fig. 13). After the change in wave forcing, the energy at $\lambda/2$ gradually decreases and the energy shifts from $\lambda/2$ to λ (Fig. 13a). The disappearance of terminations causes a slight increase in the dominant wavenumber. With respect to the interaction of the eye defect, we notice that the energy at $\lambda/2$ is higher when a small secondary crest is present (the period between the two dash-dotted lines). The increase of the energy at ripple wavelength $\lambda/2$ results in a slight variation of the energy at wavelength λ , and the energy peak slightly shifts to lower wavenumbers (longer ripple wavelength).

Interactions between defects usually occur under specific conditions (Figs. 11 and 12). For example, the eye defects usually form by the growth and migration of small secondary crests, but their formation is highly dependent on the surrounding bedform structures (Fig. 11). The presence of defects promotes bedform interactions and so is a critical aspect of the morphodynamics leading to the change in ripple wavelength towards an equilibrium geometry. This is consistent with the model from Werner and Kocurek (1999), where the defects are considered as a characteristic of bedforms, and the spacing is altered with changes in defect density. Defect interactions tend to annihilate defects, leading to longer continuous crestlines as the spacing adjusts (Werner and Kocurek, 1999).

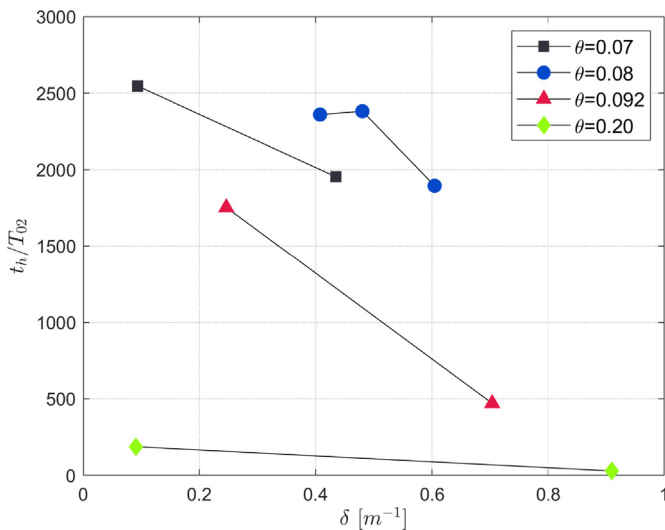


Fig. 10. Non-dimensional hysteresis versus defect density. All the points are from experiments with an increase of the Shields number. θ_{01} and θ_{02} are almost identical in each paired case. Green diamonds ($\theta_{02} = 0.2$) represent the data from Exp. 2. Red triangles ($\theta_{02} = 0.092$), black squares ($\theta_{02} = 0.08$) and blue circles ($\theta_{02} = 0.07$) are from Exp. 1.

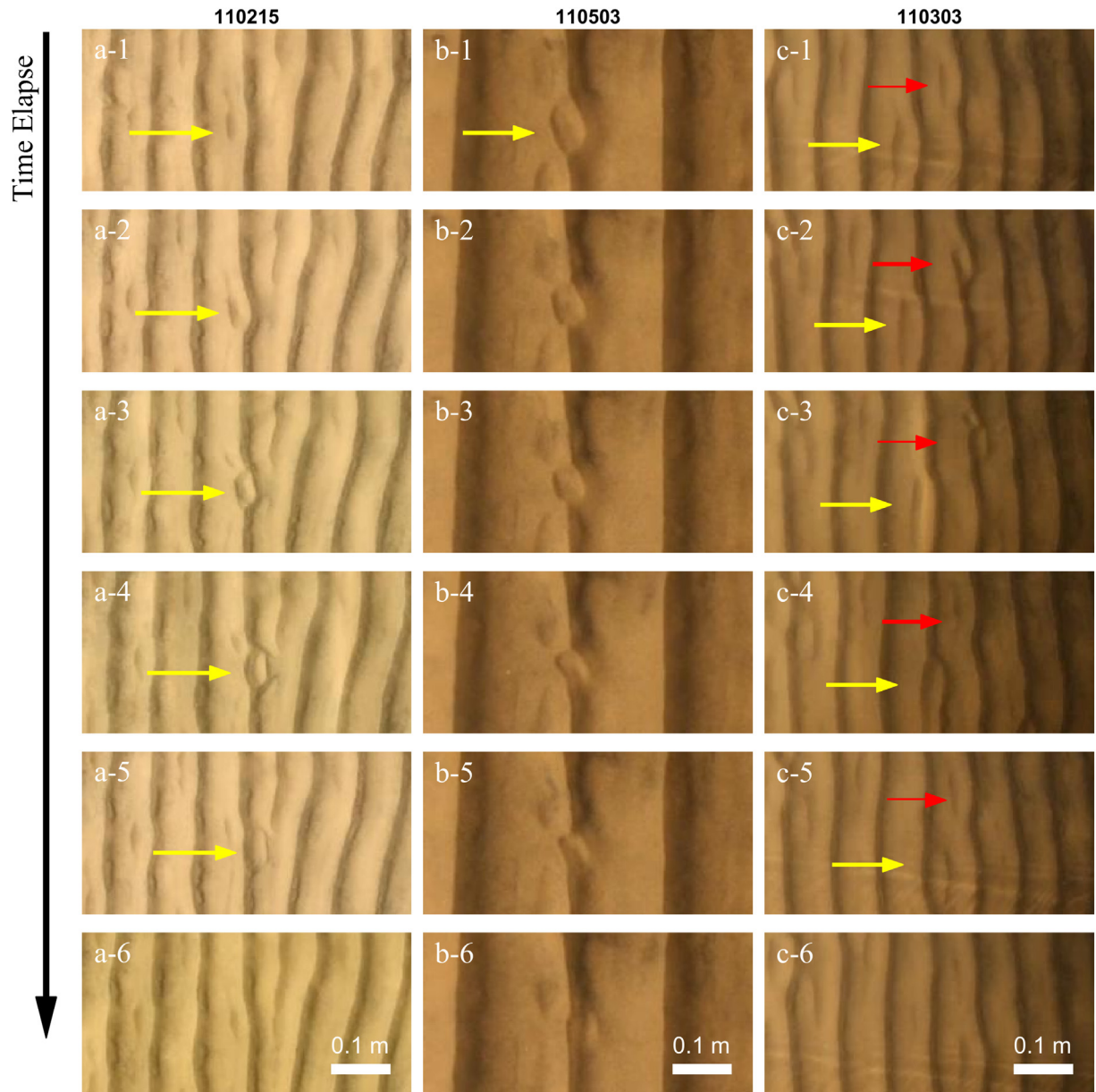


Fig. 11. Interactions between eye defects. (a) Formation and interaction of an eye defect close to a termination. (b) Formation and disappearance of an eye defect. (c) Occurrence of an eye defect as a result of defects nearby. The yellow and red arrows highlight the location of defects. The size of each image presented is 0.55 m \times 0.27 m.

4. Conclusions

Our study shows that wave orbital diameter, mobility number, Shields parameter, changes in wave orbital diameter, and defect density all influence the hysteresis of rippled beds to changes in wave conditions. In detail:

- (1) Hysteresis is proportional to the changes in wave orbital diameter, and the proportionality coefficient is larger when wave orbital diameter increases. Ripples generally adjust to changes in wave conditions that lengthen wave orbital diameter more quickly. The magnitude of change in wave orbital diameter partly accounts for the large variability in hysteresis for the same d_{02} .
- (2) Ripple adjustment does not occur below a threshold Shields parameter (0.043), which is lower than the threshold Shields parameter for sediment initiation from a flat bed (Soulis and Whitehouse, 1997). Below this lower threshold, sediment motion is active, but ripple geometry remains unchanged (or the adjustment time is longer than experiment duration).

- (3) Paired experiments with the same values of θ_{01} and θ_{02} but different defect density suggest that greater defect density results in faster ripple adjustment to equilibrium.

Declaration of competing interest

The authors declare that they have no known competing financial interests or personal relationships that could have appeared to influence the work reported in this paper.

Acknowledgements

The authors thank the editor and anonymous reviewers for their comments. Chuang Jin acknowledges the China Scholarship Council (CSC) for the support of doctoral study. Chuang Jin also thanks Dake Chen for the discussion of part of this manuscript.

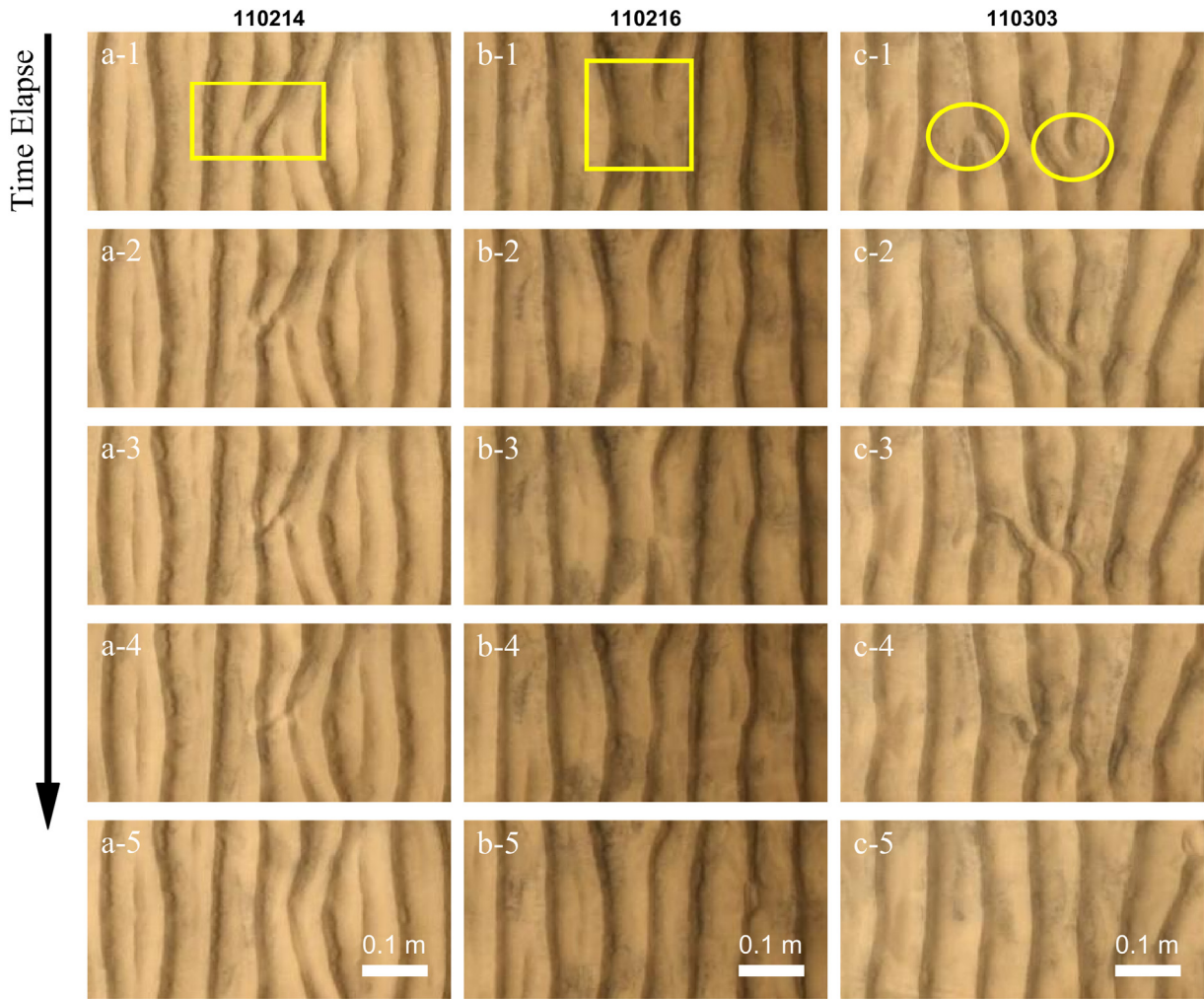


Fig. 12. Time-sequence images of interactions between terminations. The interaction occurs when two terminations are present on both sides of a distorted crestline (column a), on the same side of a crest (column b) and on both sides of two distorted crests (column c). Yellow rectangles and circles highlight the area with terminations. The size of each image presented is $0.55 \text{ m} \times 0.27 \text{ m}$.

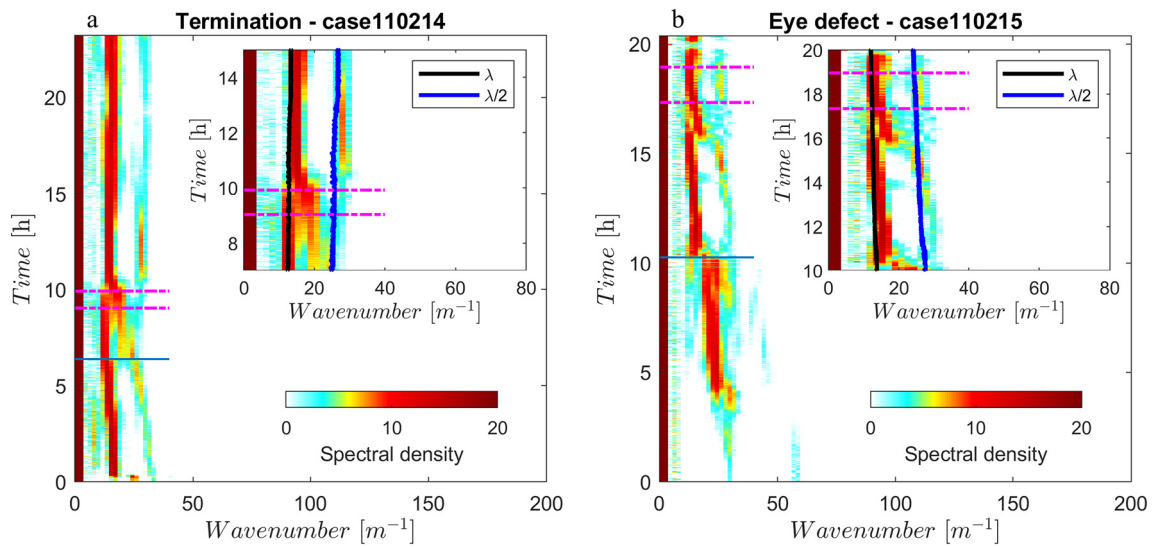


Fig. 13. Spectral density derived from cropped images (the same area as presented in Figs. 11 and 12) for (a) run 110214 (same run as Fig. 12a) and (b) run 110215 (same run as Fig. 11a) throughout the whole experiment. The light thin blue line shows the time when the wave forcing is changed. Two dash-dotted lines highlight the period when images presented in Figs. 12a and 11a are taken. Insets highlight the spectra after the change in wave forcing. The thick black and blue line show the variations of the equilibrium ripple wavelength (λ) and half the equilibrium ripple wavelength $\lambda/2$, respectively.

Appendix A. Other relevant parameters in Exp. 1 and Exp. 2

Table A1

Parameters in Exp. 1. $Re_1 = U_{m01}a_{01}/\nu$ is the Reynolds number before the change in wave conditions. $Re_2 = U_{m02}a_{02}/\nu$ is the Reynolds number after the change in wave conditions. δ_{b2} is the Stokes boundary layer thickness after the change in wave conditions.

| Run no. | Re_1 | Re_2 | d_{01}/δ_{b1} | d_{02}/δ_{b2} | D_{50}/δ_{b1} | D_{50}/δ_{b2} |
|---------|--------|--------|----------------------|----------------------|----------------------|----------------------|
| 110214 | 9540 | 7992 | 137.83 | 126.31 | 0.21 | 0.20 |
| 110215 | 3068 | 8835 | 78.14 | 132.77 | 0.24 | 0.21 |
| 110216 | 8843 | 7920 | 133.31 | 125.94 | 0.18 | 0.21 |
| 110217 | 8256 | 7830 | 128.00 | 125.31 | 0.18 | 0.21 |
| 110225 | 5240 | 8667 | 102.31 | 131.60 | 0.23 | 0.22 |
| 110226 | 9828 | 8774 | 140.37 | 132.59 | 0.20 | 0.22 |
| 110227 | 6987 | 7326 | 118.16 | 121.01 | 0.21 | 0.20 |
| 110228 | 12,528 | 7020 | 157.95 | 118.40 | 0.20 | 0.20 |
| 110301 | 14,621 | 7315 | 170.73 | 120.92 | 0.18 | 0.20 |
| 110302 | 11,680 | 9075 | 152.45 | 134.86 | 0.19 | 0.22 |
| 110303 | 4331 | 8851 | 93.00 | 132.65 | 0.24 | 0.23 |
| 110308 | 4485 | 8321 | 94.48 | 128.93 | 0.22 | 0.22 |
| 110309 | 6256 | 8507 | 111.97 | 130.63 | 0.22 | 0.22 |
| 110310 | 8349 | 5885 | 129.06 | 108.54 | 0.19 | 0.18 |
| 110314 | 12,558 | 5886 | 158.25 | 108.46 | 0.18 | 0.18 |
| 110315 | 8978 | 5565 | 134.00 | 105.94 | 0.18 | 0.18 |
| 110316 | 8127 | 5832 | 127.22 | 107.91 | 0.18 | 0.18 |
| 110317 | 4622 | 5460 | 96.14 | 104.31 | 0.22 | 0.18 |
| 110503 | 9236 | 6050 | 135.61 | 109.80 | 0.19 | 0.18 |
| 110504 | 3150 | 6813 | 79.34 | 116.63 | 0.23 | 0.19 |
| 110506 | 13,778 | 6216 | 165.95 | 111.53 | 0.18 | 0.18 |
| 110507 | 4520 | 8470 | 94.93 | 130.35 | 0.21 | 0.21 |
| 110508 | 10,488 | 6572 | 144.59 | 114.38 | 0.17 | 0.19 |
| 110510 | 4356 | 7223 | 93.36 | 120.06 | 0.19 | 0.20 |
| 110511 | 8646 | 6426 | 131.42 | 113.36 | 0.18 | 0.19 |
| 110512 | 8704 | 6649 | 131.61 | 115.02 | 0.19 | 0.19 |
| 110515 | 16,450 | 6426 | 181.74 | 113.28 | 0.17 | 0.19 |
| 110516 | 4551 | 6213 | 94.88 | 111.53 | 0.23 | 0.18 |
| 110517 | 4664 | 6260 | 96.15 | 111.47 | 0.20 | 0.19 |
| 110518 | 11,981 | 6804 | 154.61 | 116.68 | 0.17 | 0.19 |
| 120303 | 10,366 | 3080 | 143.95 | 78.45 | 0.18 | 0.25 |
| 120308 | 8107 | 3136 | 138.98 | 79.04 | 0.21 | 0.25 |
| 120312 | 10,676 | 3052 | 145.86 | 78.17 | 0.19 | 0.25 |
| 120314 | 3132 | 7729 | 79.06 | 124.39 | 0.25 | 0.19 |
| 120316 | 3248 | 7611 | 80.50 | 123.07 | 0.25 | 0.19 |
| 120320 | 2915 | 7781 | 75.93 | 124.69 | 0.26 | 0.19 |

Table A2

Parameters in Exp. 2. The symbols are the same as Table A1.

| Run no. | Re_1 | Re_2 | d_{01}/δ_{b1} | d_{02}/δ_{b2} | D_{50}/δ_{b1} | D_{50}/δ_{b2} |
|---------|--------|--------|----------------------|----------------------|----------------------|----------------------|
| Exp2-1 | 29,282 | 16,453 | 242.19 | 181.67 | 0.35 | 0.35 |
| Exp2-2 | 29,282 | 16,453 | 242.19 | 181.67 | 0.35 | 0.35 |
| Exp2-3 | 45,782 | 16,453 | 302.70 | 181.67 | 0.35 | 0.35 |
| Exp2-4 | 29,282 | 45,782 | 242.19 | 302.70 | 0.35 | 0.35 |
| Exp2-5 | 16,453 | 45,782 | 181.67 | 302.70 | 0.35 | 0.35 |
| Exp2-6 | 29,282 | 45,782 | 242.19 | 302.72 | 0.35 | 0.35 |

References

- Admiraal, D., Musalem-Jara, R., Garcia, M.H., Nino, Y., 2006. Vortex trajectory hysteresis above self-formed vortex ripples. *J. Hydraul. Res.* 44 (June 2016), 437–450. <https://doi.org/10.1080/00221686.2006.9521696>.
- Ardhuin, F., O'Reilly, W.C., Herbers, T.H.C., Jessen, P.F., 2003. Swell transformation across the Continental Shelf. Part I: attenuation and directional broadening. *J. Phys. Oceanogr.* 33 (9), 1921–1939. [https://doi.org/10.1175/1520-0485\(2003\)033<1921:STATCS>2.0.CO;2](https://doi.org/10.1175/1520-0485(2003)033<1921:STATCS>2.0.CO;2).
- Ayrton, H., 1910. The origin and growth of ripple-mark. *Proceedings of the Royal Society A: Mathematical, Physical and Engineering Sciences* 84 (571), 285–310. <https://doi.org/10.1098/rspa.1910.0076>.
- Bagnold, R.A., 1946. Motion of waves in shallow water. Interaction between waves and sand bottoms. *Proceedings of the Royal Society of London. Series A. Mathematical and Physical Sciences* 187 (1008), 1–18. <https://doi.org/10.1098/rspa.1946.0062>.
- Blondeaux, P., 1990. Sand ripples under sea waves. Part 1. Ripple formation. *J. Fluid Mech.* 218, 1–17. <https://doi.org/10.1017/S0022112001005961>.
- Charu, F., Franklin, E.M., 2012. Subaqueous barchan dunes in turbulent shear flow. Part 2. Fluid flow. *J. Fluid Mech.* 694, 131–154. <https://doi.org/10.1017/jfm.2011.528>.
- Coco, G., Murray, A.B., Green, M.O., Thielert, E.R., Hume, T.M., 2007a. Sorted bed forms as self-organized patterns: 1. Model development. *Journal of Geophysical Research: Earth Surface* 112, F03015. <https://doi.org/10.1029/2006JF000665>.
- Coco, G., Murray, A.B., Green, M.O., Thielert, E.R., Hume, T.M., 2007b. Sorted bed forms as self-organized patterns: 2. Complex forcing scenarios. *Journal of Geophysical Research: Earth Surface* 112, F03016. <https://doi.org/10.1029/2006JF000666>.
- Darwin, G.H., 1883. On the formation of ripple-mark in sand. *Proc. Roy. Soc. Lond.* 36 (228–231), 18–43. <https://doi.org/10.1098/rsp1.1883.0077>.
- Davies, A.G., Thorne, P.D., 2005. Modeling and measurement of sediment transport by waves in the vortex ripple regime. *Journal of Geophysical Research C: Oceans* 110 (5), 1–25. <https://doi.org/10.1029/2004JC002468>.
- Dimas, A.A., Leftheriotis, G.A., 2019. Mobility parameter and sand grain size effect on sediment transport over vortex ripples in the orbital regime. *Journal of Geophysical Research: Earth Surface* 124 (1), 2–20. <https://doi.org/10.1029/2018JF004741>.
- Doucette, J.S., O'Donoghue, T., 2006. Response of sand ripples to change in oscillatory flow. *Sedimentology* 53 (3), 581–596. <https://doi.org/10.1111/j.1365-3091.2006.00774.x>.
- Fredsoe, J., Andersen, K.H., Mutlu Sumer, B., 1999. Wave plus current over a ripple-covered bed. *Coast. Eng.* 38 (4), 177–221. [https://doi.org/10.1016/S0378-3839\(99\)00047-2](https://doi.org/10.1016/S0378-3839(99)00047-2).

- Goldstein, E.B., Coco, G., Murray, A.B., 2013. Prediction of wave ripple characteristics using genetic programming. *Cont. Shelf Res.* 71, 1–15. <https://doi.org/10.1016/j.csr.2013.09.020>.
- Grant, W.D., Madsen, O.S., 1982. Movable bed roughness in unsteady oscillatory flow. *J. Geophys. Res.* 87 (C1), 469–481. <https://doi.org/10.1029/JC087iC01p00469>.
- Green, M.O., Black, K.P., 1999. Suspended-sediment reference concentration under waves: field observations and critical analysis of two predictive models. *Coast. Eng.* 38 (3), 115–141. [https://doi.org/10.1016/S0378-3839\(99\)00044-7](https://doi.org/10.1016/S0378-3839(99)00044-7).
- Hansen, J.L., Van Hecke, M., Ellegaard, C., Andersen, K.H., Bohr, T., Haaning, A., Sams, T., 2001a. Stability balloon for two-dimensional vortex ripple patterns. *Phys. Rev. Lett.* 87 (20), 204301. <https://doi.org/10.1103/PhysRevLett.87.204301>.
- Hansen, J.L., Van Hecke, M., Haaning, A., Ellegaard, C., Andersen, K.H., Bohr, T., Sams, T., 2001b. Pattern formation: instabilities in sand ripples. *Nature* 410 (6826), 324. <https://doi.org/10.1038/35066631>.
- Huntley, D.A., Coco, G., Bryan, K.R., Murray, A.B., 2008. Influence of “defects” on sorted bedform dynamics. *Geophys. Res. Lett.* 35 (2), L02601. <https://doi.org/10.1029/2007GL030512>.
- Jerolmack, D., Mohrig, D., 2005. Interactions between bed forms: topography, turbulence, and transport. *Journal of Geophysical Research: Earth Surface* 110 (2), 1–13. <https://doi.org/10.1029/2004JF000126>.
- Jin, C., Coco, G., Tinoco, R.O., Goldstein, E.B., Gong, Z., 2019. Laboratory experiments on the role of hysteresis, defect dynamics and initial perturbation on wave-generated ripple development. *Estuar. Coast. Shelf Sci.* 224, 142–153. <https://doi.org/10.1016/j.ecss.2019.05.003>.
- Kocurek, G., Ewing, C.R., Mohrig, D., 2010. How do bedform patterns arise? New views on the role of bedform interactions within a set of boundary conditions. *Earth Surf. Process. Landf.* 35 (1), 51–63. <https://doi.org/10.1002/esp.1913>.
- Mariou, V., Bonneton, P., Foster, D.L., Ardhuin, F., 2008. Modeling of vortex ripple morphodynamics. *Journal of Geophysical Research: Oceans* 113 (9), 1–15. <https://doi.org/10.1029/2007JC004659>.
- Mazzuoli, M., Blondeaux, P., Simeonov, J., Calantoni, J., 2018. Direct numerical simulation of oscillatory flow over a wavy, rough, and permeable bottom. *Journal of Geophysical Research: Oceans* 123 (3), 1595–1611. <https://doi.org/10.1002/2017JC013447>.
- Mazzuoli, M., Kidanemariam, A.G., Uhlmann, M., 2019. Direct numerical simulations of ripples in an oscillatory flow. *J. Fluid Mech.* 863, 572–600. <https://doi.org/10.1017/jfm.2018.1005>.
- Mazzuoli, M., Blondeaux, P., Vittori, G., Uhlmann, M., Simeonov, J., Calantoni, J., 2020. Interface-resolved direct numerical simulations of sediment transport in a turbulent oscillatory boundary layer. *J. Fluid Mech.* 885 (A28), 1–31. <https://doi.org/10.1017/jfm.2019.1012>.
- Miller, M.C., Komar, P.D., 1980. A field investigation of the relationship between oscillation ripple spacing and the near-bottom water orbital motions. *J. Sediment. Res.* 50 (1), 183–191. <https://doi.org/10.2110/jsr.50.183>.
- Mogridge, G.R., Davies, M.H., Willis, D.H., 1994. Geometry prediction for wave-generated bedforms. *Coast. Eng.* 22 (3–4), 255–286. [https://doi.org/10.1016/0378-3839\(94\)90039-6](https://doi.org/10.1016/0378-3839(94)90039-6).
- Myrow, P.M., Jerolmack, D.J., Perron, J.T., 2018. Bedform disequilibrium. *J. Sediment. Res.* 88 (9), 1096–1113. <https://doi.org/10.2110/jsr.2018.55>.
- Nelson, T.R., Voulgaris, G., 2014. Temporal and spatial evolution of wave-induced ripple geometry: regular versus irregular ripples. *Journal of Geophysical Research: Oceans* 119 (2), 664–688. <https://doi.org/10.1002/2013JC009020>.
- Nelson, T.R., Voulgaris, G., 2015. A spectral model for estimating temporal and spatial evolution of rippled seabeds. *Ocean Dyn.* 65 (2), 155–171. <https://doi.org/10.1007/s10236-014-0801-y>.
- Nielsen, P., 1981. Dynamics and geometry of wave-generated ripples. *J. Geophys. Res.* 86 (C7), 6467–6472. <https://doi.org/10.1029/JC086iC07p06467>.
- Nienhuis, J.H., Perron, J.T., Kao, J.C.T., 2014. Wavelength selection and symmetry breaking in orbital wave ripples. *Journal of Geophysical Research: Earth Surface* 119, 2239–2257. <https://doi.org/10.1002/2014JF003158>.
- Önder, A., Yuan, J., 2019. Turbulent dynamics of sinusoidal oscillatory flow over a wavy bottom. *J. Fluid Mech.* 858, 264–314. <https://doi.org/10.1017/jfm.2018.754>.
- Pedocchi, F., García, M.H., 2009. Ripple morphology under oscillatory flow: 2. Experiments. *Journal of Geophysical Research: Oceans* 114 (12), 1–17. <https://doi.org/10.1029/2009JC005356>.
- Perillo, M.M., Prokocki, E.W., Best, J.L., García, M.H., 2014. Bed form genesis from bed defects under unidirectional, oscillatory, and combined flows. *Journal of Geophysical Research: Earth Surface* 119 (12), 2635–2652. <https://doi.org/10.1002/2014JF003167>.
- Perron, J.T., Myrow, P., Southard, J.B., Huppert, K.L., Szulczewski, M., 2010. Defect dynamics in wave ripples. *AGU Fall Meeting Abstracts*.
- Perron, J.T., Myrow, P.M., Huppert, K.L., Koss, A.R., Wickert, A., 2016. Wave ripple time-lapse experiments. *SEAD Internal Repository* <https://doi.org/10.5967/M0QR4V39>.
- Perron, J.T., Myrow, P.M., Huppert, K.L., Koss, A.R., Wickert, A.D., 2018. Ancient record of changing flows from wave ripple defects. *Geology* 46 (10), 875–878. <https://doi.org/10.1130/G45463.1>.
- Ruessink, G., Brinkkemper, J., Kleinhans, M., 2015. Geometry of wave-formed orbital ripples in coarse sand. *Journal of Marine Science and Engineering* 3 (4), 1568–1594. <https://doi.org/10.3390/jmse3041568>.
- Seikiguchi, T., Sunamura, T., 2004. A laboratory study of formative conditions for characteristic ripple patterns associated with a change in wave conditions. *Earth Surf. Process. Landf.* 29 (11), 1431–1435. <https://doi.org/10.1002/esp.1139>.
- Skarke, A., Trembanis, A.C., 2011. Parameterization of bedform morphology and defect density with fingerprint analysis techniques. *Cont. Shelf Res.* 31 (16), 1688–1700. <https://doi.org/10.1016/j.csr.2011.07.009>.
- Smith, D., Sleath, J.F.A., 2005. Transient ripples in oscillatory flows. *Cont. Shelf Res.* 25 (4), 485–501. <https://doi.org/10.1016/j.csr.2004.10.012>.
- Soulsby, R.L., Whitehouse, R.J.S., 1997. Threshold of sediment motion in coastal environments. *Proceedings of the Pacific Coasts and Ports 1997 Conference. Centre for Advanced Engineering, Christchurch, NZ.*
- Soulsby, R.L., Whitehouse, R.J.S., Marten, K.V., 2012. Prediction of time-evolving sand ripples in shelf seas. *Cont. Shelf Res.* 38, 47–62. <https://doi.org/10.1016/j.csr.2012.02.016>.
- Styles, R., Glenn, S., 2002. Modeling bottom roughness in the presence of wave-generated ripples. *J. Geophys. Res.* 107 (C8), 24–1. <https://doi.org/10.1029/2001JC000864>.
- Swart, D.H., 1974. *Offshore sand transport and equilibrium beach profiles. Delft Hydraulics Publication. vol. 131. Delft Hydraulics, The Netherlands.*
- Testik, F.Y., Voropayev, S.I., Fernando, H.J.S., 2005. Adjustment of sand ripples under changing water waves. *Phys. Fluids* 17 (7), 1–8. <https://doi.org/10.1063/1.1946768>.
- Traykovski, P., 2007. Observations of wave orbital scale ripples and a nonequilibrium time-dependent model. *Journal of Geophysical Research: Oceans* 112 (6), 1–19. <https://doi.org/10.1029/2006JC003811>.
- Traykovski, P., Hay, A.E., Irish, J.D., Lynch, J.F., 1999. Geometry, migration, and evolution of wave orbital ripples at LEO-15. *Journal of Geophysical Research: Oceans* 104 (C1), 1505–1524. <https://doi.org/10.1029/1998JC900026>.
- Van der Werf, J.J., Doucette, J.S., O'Donoghue, T., Ribberink, J.S., 2007. Detailed measurements of velocities and suspended sand concentrations over full-scale ripples in regular oscillatory flow. *Journal of Geophysical Research: Earth Surface* 112 (2), 1–18. <https://doi.org/10.1029/2006JF000614>.
- Van Rijn, L.C., 1993. *Principles of Sediment Transport in Rivers, Estuaries and Coastal Seas. Aqua Publications, Amsterdam.*
- Wang, D., Yuan, J., 2019. Geometric characteristics of coarse-sand ripples generated by oscillatory flows: a full-scale experimental study. *Coast. Eng.* 147, 159–174. <https://doi.org/10.1016/j.coastaleng.2019.02.007>.
- Werner, B.T., Kocurek, G., 1997. Bed-form dynamics: does the tail wag the dog? *Geology* 25 (9), 771–774. [https://doi.org/10.1130/0091-7613\(1997\)025<0771:BFDDTT>2.3.CO](https://doi.org/10.1130/0091-7613(1997)025<0771:BFDDTT>2.3.CO).
- Werner, B.T., Kocurek, G., 1999. Bedform spacing from defect dynamics. *Geology* 27 (8), 727–730. [https://doi.org/10.1130/0091-7613\(1999\)027<0727:BSFDD>2.3.CO](https://doi.org/10.1130/0091-7613(1999)027<0727:BSFDD>2.3.CO).
- Wiberg, P.L., Harris, C.K., 1994. Ripple geometry in wave-dominated environments. *J. Geophys. Res.* 99 (C1), 775–789. <https://doi.org/10.1029/93JC02726>.
- Wu, X., Parsons, D.R., 2019. Field investigation of bedform morphodynamics under combined flow. *Geomorphology* 339, 19–30. <https://doi.org/10.1016/j.geomorph.2019.04.028>.
- Wu, X., Baas, J.H., Parsons, D.R., Eggenhuisen, J., Amoudry, L., Cartigny, M., McLelland, S., Mouazé, D., Ruessink, G., 2018. Wave ripple development on mixed Clay-sand substrates: effects of clay winnowing and armoring. *Journal of Geophysical Research: Earth Surface* 123 (11), 2784–2801. <https://doi.org/10.1029/2018JF004681>.
- Yuan, J., Wang, D., 2018. Experimental investigation of total bottom shear stress for oscillatory flows over sand ripples. *Journal of Geophysical Research: Oceans* 123 (9), 6481–6502. <https://doi.org/10.1029/2018JC013953>.
- Zgheib, N., Fedele, J.J., Hoyal, D.C.J.D., Perillo, M.M., Balachandrar, S., 2018a. Direct numerical simulation of transverse ripples: 1. Pattern initiation and bedform interactions. *Journal of Geophysical Research: Earth Surface* 123 (3), 448–477. <https://doi.org/10.1002/2017JF004398>.
- Zgheib, N., Fedele, J.J., Hoyal, D.C.J.D., Perillo, M.M., Balachandrar, S., 2018b. Direct numerical simulation of transverse ripples: 2. Self-similarity, bedform coarsening, and effect of neighboring structures. *Journal of Geophysical Research: Earth Surface* 123 (3), 478–500. <https://doi.org/10.1002/2017JF004399>.